10536 Inorg. Chem. 2010, 49, 10536–10542
DOI: 10.1021/ic1015669

Inorganic Chemistry
Article

$Ru_9Zn_7Sb_8$: A Structure with a 2 × 2 × 2 Supercell of the Half-Heusler Phase

Ding-Bang Xiong,*[†,‡] Yufeng Zhao,[†] Norihiko L. Okamoto,[‡] Clemens Pietzonka,[†] Takeshi Waki,[‡] and Haruyuki Inui[‡]

[†]Department of Chemistry and Center of Material Sciences, Philipps University Marburg, Hans-Meerwein-Strasse, 35032 Marburg, Germany, and [‡]Department of Materials Science and Engineering, Kyoto University, Kyoto 606-8501, Japan

Received August 3, 2010

The title compound $Ru_9Zn_7Sb_8$ was synthesized via a high-temperature reaction from the elements in a stoichiometric ratio, and its structure was solved by a single-crystal X-ray diffraction method. The structure [cubic, space group $Fm\bar{3}m$, Pearson symbol $cF96$, $a = 11.9062(14)$ Å (293 K), and $Z = 4$] adopts a unique $2a_{hh} \times 2a_{hh} \times 2a_{hh}$ supercell of a normal half-Heusler phase and shows abnormal features of atomic coordination against the Pauling rule. The formation of this superstructure was discussed in light of the valence electron concentration per unit cell. It is a metallic conductor [$\rho(300\ K) = 16\ \mu\Omega\cdot m$], and differential scanning calorimetry revealed that $Ru_9Zn_7Sb_8$ undergoes a transformation at 1356(1) K and melts, by all indications, congruently at 1386 K. At room temperature, its thermal conductivity is about 3 W/m·K, which is only one-quarter of that of most normal half-Heusler phases. $Ru_9Zn_7Sb_8$ as well as its analogues of iron-, cobalt-, rhodium-, and iridium-containing compounds are expected to serve as a new structure type for exploring new thermoelectric materials.

Introduction

Half-Heusler phases are chemically versatile and rich in physical properties. They are considered as a promising class of multifunctional materials with potential application in spin-controlled electron transport,[1] thermoelectrical energy conversion,[2] magnetic shape memory,[3] superconductivity,[4] and topological insulation.[5] Half-Heusler compounds represent one of the prominent groups[6] of equiatomic ternary compounds XYZ (space group, $F\bar{4}3m$, and Pearson symbol $cF12$), where X and Y are usually transition metals, whereas Z is an sp-valent element. The Z component forms a cubic-close-packed arrangement, with X occupying all of octahedral sites and Y half of the tetrahedral sites. The pattern of how the tetrahedral sites are occupied conforms to the principle of maximal self-avoidance. Hence, the half-Heusler structure type is also referred to as a stuffed zinc blende type structure. Hexagonal counterparts are known as well, such as ScCuSn.[7] Moreover, half-Heusler compounds can be classified according to the number of valence electrons per formula unit provided by its constituents. A structure map, shown in Figure 1, reveals that half-Heusler structures with various valence electron concentrations (VECs) are formed. However, the fact that no phases with electrons between 8 and 16 have been known makes it challenging to search for possible phases in those gaps. Herein, we report a phase $Ru_9Zn_7Sb_8$ in which its composition deviates from the equiatomic XYZ in a normal half-Heusler phase. $Ru_9Zn_7Sb_8$ forms a unique $2a_{hh} \times 2a_{hh} \times 2a_{hh}$ superstructure of a normal half-Heusler phase (a_{hh} refers to the cubic lattice parameter of a normal half-Heusler structure), in which each half-Heusler type subunit exhibits 15.75 valence electrons. If the distinctive composition is disregarded, the structure $Ru_9Zn_7Sb_8$ is related to that of CoMnSb, which has been recently identified by means of powder X-ray diffraction (XRD).[8]

Experimental Section

Synthesis and Phase Characterization. All samples were prepared on about a 300 mg scale via a high-temperature reaction of

---

*To whom correspondence should be addressed. E-mail: dingbang.xiong@ky8.ecs.kyoto-u.ac.jp.

[1] (1) Katsnelson, M. I.; Irkhin, V. Yu.; Chioncel, L.; Lichtenstein, A. I.; de Groot, R. A. *Rev. Mod. Phys.* **2008**, *80*, 315. (b) Felser, C.; Fecher, G. H.; Balke, B. *Angew. Chem., Int. Ed.* **2007**, *46*, 668. (c) Kammerer, S.; Thomas, A.; Hutten, A.; Reiss, G. *Appl. Phys. Lett.* **2004**, *85*, 79.

[2] (2) (a) Yang, J.; Li, H. M.; Wu, T.; Zhang, W. Q.; Chen, L. D.; Yang, J. H. *Adv. Funct. Mater.* **2008**, *18*, 2880. (b) Nolas, G. S.; Poon, J.; Kanatzidis, M. *MRS Bull.* **2006**, *31*, 199. (c) Uher, C.; Yang, J.; Hu, S.; Morelli, D. T.; Meisner, G. P. *Phys. Rev. B* **1999**, *59*, 8615.

[3] (3) (a) Kainuma, R.; Oikawa, K.; Ito, W.; Sutou, Y.; Kanomata, T.; Ishida, K. *J. Mater. Chem.* **2008**, *18*, 1837. (b) Kainuma, R.; Imano, Y.; Ito, W.; Sutou, Y.; Morito, H.; Okamoto, S.; Kitakami, O.; Oikawa, K.; Fujita, A.; Kanomata, T.; Ishida, K. *Nature* **2006**, *439*, 957.

[4] (4) Goll, G.; Marz, M.; Hamann, A.; Tomanic, T.; Grube, K.; Yoshino, T.; Takabatake, T. *Physica B* **2008**, *403*, 1065.

[5] (5) (a) Chadov, S.; Qi, X. L.; Kübler, J.; Fecher, G. H.; Felser, C.; Zhang, S. C. *Nat. Mater.* **2010**, *9*, 541. (b) Lin, H.; Wray, L. A.; Xia, Y. Q.; Xu, S. Y.; Jia, S.; Cava, R. J.; Bansil, A.; Hasan, M. Z. *Nat. Mater.* **2010**, *9*, 546.

[6] (6) Bojin, M. D.; Hoffmann, R. *Helv. Chim. Acta* **2003**, *86*, 1653 and 1683.

[7] (7) Casper, F.; Felser, C.; Seshadri, R.; Sebastian, C. P.; Pöttgen, R. *J. Phys. D: Appl. Phys.* **2008**, *41*, 035002.

[8] (8) Ksenofontov, V.; Melnyk, G.; Wojcik, M.; Wurmehl, S.; Kroth, K.; Reiman, S.; Blaha, P.; Felser, C. *Phys. Rev. B* **2006**, *74*, 134426.

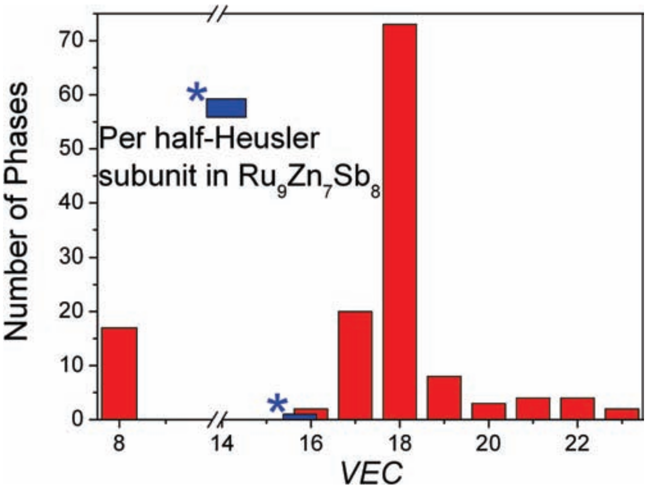

Figure 1. Histogram of VEC values for reported cubic half-Heusler phases. The total number of phases included in this histogram is 133.

Table 1. Crystallographic and Technical Data of the Single-Crystal Structure Refinement of $Ru_9Zn_7Sb_8$

chemical formula	$Ru_9Zn_7Sb_8$
M_r	2341.22
space group (No.), Z	$Fm\bar{3}m$, 4
Pearson symbol	*cF*96
a/Å	11.9062(14)
V/Å^3	1687.8(3)
D_c/(g/cm^3)	9.21
μ/mm^{-1}	30.04
θ_{max}/deg	32.95
reflns measd	6026
index range, *hkl*	−18 to +18, −18 to +18, −18 to +17
min/max transmn	0.0295/0.0685
unique reflns	202
R_{int}	0.0472
no. of used reflns	202
no. of variables	14
obsd reflns [$I_0 > 2\sigma(I_0)$]	201
$R(F)$ [a] [$I_0 > 2\sigma(I_0)$]	0.0244
$R(F)$ (all data)	0.0246
$wR(F^2)$ [b] (all data)	0.0566
GOF (F^2)	1.520
$\Delta\rho_{min}/\Delta\rho_{max}/10^{-6}$ e/pm^3	−0.814/1.231

[a] $R = \sum||F_o| - |F_c||/\sum|F_o|$. [b] $wR = \{\sum[w(F_o^2 - F_c^2)^2]/\sum[w(F_o^2)^2]\}^{1/2}$.

Table 2. Atomic Coordinates and Equivalent Displacement Parameters (Å^2) for $Ru_9Zn_7Sb_8$

atom	site	symmetry	*x*	*y*	*z*	U_{eq} [a]
Sb1	8c	−43*m*	$^1/_4$	$^1/_4$	$^1/_4$	0.0071(3)
Sb2	24e	4*mm*	0.27405(7)	0	0	0.0092(2)
Ru1	4b	*m*−3*m*	$^1/_2$	0	0	0.0057(4)
Ru2	32f	0.3*m*	0.12298(4)	0.12298(4)	0.12298(4)	0.0090(2)
Zn1	4a	*m*−3*m*	0	0	0	0.0071(6)
Zn2	24d	*mmm*	0	$^1/_4$	$^1/_4$	0.0115(3)

[a] U_{eq} is defined as one-third of the trace of the orthogonalized U_{ij} tensor.

ruthenium (Degussa, 99.9%), zinc (Chempur, 99.99%), and antimony (99.8%) in evacuated fused-silica tubes. The samples were typically heated to 1323 K at a rate of 80 K/h, maintained at 1323 K for 6 h, then cooled to 1173 K at a rate of 25 K/h, and maintained at 1173 K for 4 days. Thereafter, the ampules were taken out from the furnace and cooled to room temperature in air. In order to avoid the loss of zinc and antimony due to condensation outside the reaction zone, the reactants were placed at the least hot site of the ampules, and the furnace was placed on at a small slope to make sure the elements contact thoroughly. The chemical compositions of selected samples were examined in a scanning electron microscope (CS 4DV, CamScan) equipped with an energy-dispersive X-ray spectrometer [Si(Li) detector, Noran Instruments].

Crystal Structure Determination. The crystal structure was studied by single-crystal XRD. The diffraction intensities were recorded with an image plate diffractometer (Stoe & Cie) operating with Mo Kα radiation (λ = 0.710 69 Å) at 293 K. The diffraction peaks were conclusively indexed on the basis of a face-centered-cubic unit cell. Numerical absorption corrections based on the sizes and shapes of the crystals were applied to the data sets with the programs *X-SHAPE*[9] and *X-RED*.[10] The structures were solved in the space group $Fm\bar{3}m$ (No. 225) by applying direct methods and subsequently refined on F^2 with a full-matrix least-squares algorithm with the aid of the program *SHELXTL*, version 6.1.[11] At the first stage, the refinement converged smoothly with $R(F)$ values smaller than 5% and gave a composition of $Ru_9Zn_7Sb_8$, and the structure was subsequently refined with anisotropic displacement parameters. The site occupations were checked by freeing the site occupancy factor (SOF) of an individual atomic site while keeping the remaining SOFs fixed. Finally, least-squares refinements with anisotropic parameters converged at R1 = wR2 = 5.66%, GOF = 1.52 for 14 parameters and 201 independent reflections [$I > 2\sigma(I)$]. Additional details concerning data collection and crystallographic data, atomic coordinates, and interatomic distances are summarized in Tables 1−3. Further details of the crystal structure investigations can be obtained from Fachinformationszentrum Karlsruhe, D-76344 Eggenstein-Leopoldshafen, Germany [fax (+49) 7247-808-666; e-mail crysdata@fiz.karlsruhe.de] on quoting the depository number CSD 421339.

Mössbauer Spectroscopy. ^{121}Sb Mössbauer measurements were performed with a constant-acceleration Mössbauer spectrometer in a standard transmission geometry using a ^{121m}Sn ($CaSnO_3$) source with a nominal activity of 3 mCi. To increase the recoil-free fraction, both the source and the absorber were immersed in liquid helium. The spectra were analyzed using the transmission integral in the EFFI program. As a constraint, the recoil-free fraction of the source was kept to 0.7.

Physical Property Measurements. The temperature dependence of the electrical resistivity of $Ru_9Zn_7Sb_8$ was determined in the temperature range from 2 to 660 K for a hot-pressed powder sample. The density of the as-produced specimen is about 76% of the theoretical value. Below room temperature, the electrical resistivity was measured by the four-probe method with an applied electrical current of 0.1 mA. Above room temperature, the electrical resistivity and Seebeck coefficient were measured with an ULVAC ZEM-2 apparatus in a helium atmosphere up to 660 K. The specific heat capacity (C_p) at room temperature and thermal diffusivity (α) up to 670 K were collected by the laser flasher method with an ULVAC TC-7000 apparatus for thin-disk specimens with a diameter of 10 mm and a thickness of 1 mm.

The thermal stability was studied in the temperature range from 673 to 1395 K using a differential scanning calorimeter (setsys 16/18, Setaram). The sample was pressed into pellets (∼33 mg). The pellets were sealed in evacuated silica crucibles, which were repeatedly heated and cooled at a rate of 0.17 K/s (four cycles) in order to produce an approximate thermal-balanceable process. The first two cycles were run from 673 to 1323 K and the last two from 673 to 1395 K. There are not any visible exo- or endothermal peaks in the first two cycles, and the results from cycles 3 and 4 are shown in Figure S3 (Supporting Information).

Magnetic susceptibility measurements were carried out with the aid of a SQUID magnetometer (MPMS, Quantum Design). The data were corrected for diamagnetic contributions from

---

(9) *X-SHAPE: Crystal Optimization for Numerical Absorption Correction*, version 2.01; Sote & Cie: Darmstadt, Germany, 2001.

(10) *X-RED: Data Reduction Program*, version 1.02; Stoe & Cie: Darmstadt, Germany, 2001.

(11) Sheldrick, G. M. *SHELXTL Programs*, release version 6.10; Bruker AXS: Madison, WI, 1998.

Table 3. Interatomic Distances (Å) in the Structure of $Ru_9Zn_7Sb_8$

Sb1−Ru2 × 4	2.6194(8)	Ru1−Sb2 × 6	2.6901(8)	Zn1−Ru2 × 8	2.5361(8)
Zn2 × 6	2.9766(4)	Ru2−Zn1	2.5361(8)	Sb2 × 6	3.2630(4)
Sb2−Ru1	2.6901(9)	Zn2 × 3	2.5902(4)	Zn2−Ru2 × 4	2.5920(4)
Ru2 × 4	2.7429(6)	Sb1	2.6194(8)	Sb1 × 2	2.9766(4)
Zn2 × 4	2.9903(4)	Sb2 × 3	2.7429(6)	Sb2 × 4	2.9903(4)
		Ru2 × 3	2.9284(10)		

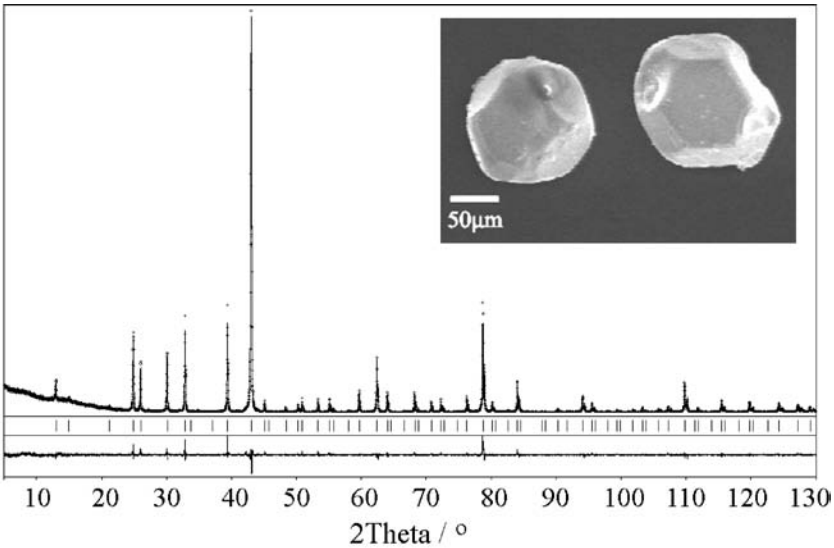

Figure 2. Powder XRD pattern and a Rietveld profile fit of $Ru_9Zn_7Sb_8$ (top). Measured (dots) and calculated (line) intensities with a difference plot (bottom). In the middle, the positions of the Bragg angles of $Ru_9Zn_7Sb_8$ are shown. The refined lattice parameter $a = 11.90952(5)$ Å is in good agreement with that determined on a single crystal, $a = 11.9062(14)$ Å. The inset is the scanning electron micrograph of the as-produced $Ru_9Zn_7Sb_8$.

a sample holder manufactured from Teflon. Powdered samples of 150−300 mg with different purities were loaded into the sample holder. Magnetization measurements for normal-state properties were carried out between 2 and 350 K in fields of 50 kG. For superconducting-state properties, measurements with an external field of 50−400 G between 5 and 8 K were carried out with field cooling and zero-field cooling of the samples.

Electronic Structure Calculation. To assess the chemical bonding and structural stability, electronic band structure calculations for $Ru_9Zn_7Sb_8$ were performed within the local density approximation[12] using the linear muffin-tin orbital (LMTO) method[13] encoded in the *TB-LMTO-ASA* program.[14] All k-space integrations were performed with the tetrahedron method using 512k points within the Brillouin zone.[15] The basis set consists of 3d/4s/4p, 5s/5p, and 4d/5s/5p orbitals for Zn, Sb, and Ru, respectively. The 5d/4f orbitals for Sb and the 5f orbitals for Ru were dealt with the downfolding technique,[16] treating the inner electrons as a soft core. Our calculations did not include spin−orbit coupling and treated the relativistic effects in terms of the scalar relativistic method. For a sufficiently large overlap of the atomic spheres, it was necessary to insert one empty sphere into the interstitial regions. To examine the chemical bonding in $Ru_9Zn_7Sb_8$ in more detail, we also performed crystal orbital Hamiltonian population (COHP) analysis,[17] which partitions the band-structure energy (i.e., the sum of the Kohn−Sham orbital energies) into contributions between pairs of atomic orbitals. All COHP plots are presented under the convention in which positive and negative values refer to bonding and antibonding interactions, respectively.

Results and Discussion

$Ru_9Zn_7Sb_8$ was prepared via a high-temperature reaction from the elements in a stoichiometric ratio, and its structure was determined by fitting the Rietveld profile to a powder XRD pattern of pristine $Ru_9Zn_7Sb_8$ (Figure 2 and also Table S3 in the Supporting Information). Single-crystal X-ray analysis revealed that the crystal structure belongs to the $Fm\bar{3}m$ space group symmetry and contains 96 atoms per unit cell. It is not easy to control the phase purity, and it strongly depends on the balance of the volume size of the as-sealed silica tube and the applied temperature program. As indicated by the results of energy-dispersive X-ray spectrometry (EDS) and single-crystal XRD (Tables S1 and S2 in the Supporting Information) on the different samples, this structure can exist at least in the solid solution range $Ru_{9-x}Zn_{7+x}Sb_8$ $(0 \leq x \leq 1)$.

According to the single-crystal structure refinement, $Ru_9Zn_7Sb_8$ is built up of six different crystallographic sites, four of which are located at special sites, yet not so Ru2 and Sb2 sites (Figure 3b). The positional parameters are given in Table 2. Sb1 (8c) and Sb2 (24e) form a slightly distorted cubic-closed-packed arrangement of atoms. Zn1 (4a), Zn2 (24d), and Ru1 (4b) occupy all of the octahedral sites, while Ru2 (32f) occupies the tetrahedral sites. The normal half-Heusler phase XYZ (Figure 3a) differs from the half-Heusler type subunit $Ru_{4.5}Zn_{3.5}Sb_4$ $[Ru_{(4+4/8)}Zn_{(6/2+4/8)}Sb_{(1+12/4)}]$ in such a way that half of the Y atoms at the eight corners of the cubic unit cell were replaced by X atoms, and here Zn was replaced by Ru.

---

[12] Barth, U. V.; Hedin, L. *J. Phys. C* **1972**, *5*, 1629.

[13] (a) Andersen, O. K. *Phys. Rev. B* **1975**, *12*, 3060. (b) Andersen, O. K.; Jepsen, O. *Phys. Rev. Lett.* **1984**, *53*, 2571. (c) Andersen, O. K.; Arcangeli, C.; Tank, R. W.; Saha-Dasgupta, T.; Krier, G.; Jepsen, O.; Dasgupta, I. *Mater. Res. Soc. Symp. Proc.* **1998**, *491*, 3.

[14] Krier, G.; Jepsen, O.; Burkhardt, A.; Andersen, O. K. *The TB-LMTO-ASA program*, version 4.7.

[15] Jepsen, O.; Andersen, O. K. *Solid State Commun.* **1971**, *9*, 1763.

[16] Jepsen, O.; Andersen, O. K.; Snob, M. In *Linearized Band-Structure Method in Electronic Band Structure and its Applications*; Lecture Notes in Physics; Springer: Berlin, 1987.

[17] Dronskowski, R.; Blöchl, P. E. *J. Phys. Chem.* **1993**, *97*, 8617.

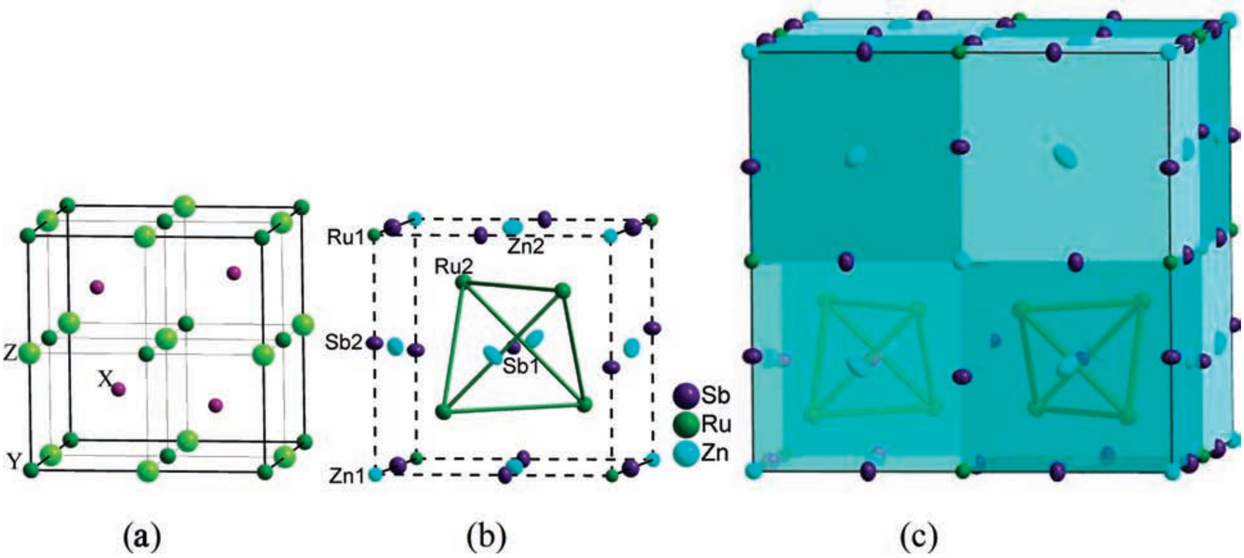

Figure 3. (a) Crystal structure of the normal half-Heusler XYZ. Replacing half of the X atoms at cubic corners with Y atoms leads to a half-Heusler-type subunit (b) in $Ru_9Zn_7Sb_8$ (c), showing a $2a_{hh} \times 2a_{hh} \times 2a_{hh}$ superstructure of the half-Heusler-type structure. Blue and light-blue subunits in part c represent the same half-Heusler subunits in part b but with different orientations. Thermal ellipsoids are at the 90% probability level.

As shown in Figure 3c, when deviation in the composition is neglected, the unique structure with a doubled a_{hh} lattice parameter corresponds to a coherently ordered inversion twin of an ordinary half-Heusler phase. If the origin of the unit cell is shifted by $^1/_8$ along its body diagonals, as shown in Figure 4, the structure can also be considered as an alternation of face-sharing full-Heusler-type Ru_2ZnSb and NaCl-type $(RuZn_3)Sb_4$ subunits.

What is accompanied with the doubling of the lattice parameter is the increase in the degrees of freedom in the positional parameters for Sb2 and Ru2 causing specific distortions. The positional parameters as well as the lattice parameter are optimized to achieve the lowest energy state or local minimum energy. Taking an undistorted structure as a reference ($x_{Ru2} = {}^1/_8$ instead of 0.12298; $x_{Sb2} = {}^1/_4$ instead of 0.27405), the displacements, if atomic radii ($r_{Ru} = 1.325$ Å, $r_{Zn} = 1.335$ Å, and $r_{Sb} = 1.45$ Å, in the Bragg−Slater scale)[18] are also taken into account, may provide hints about the specific bonding interaction. The shortest interatomic distances (Table 2) are compared with those of an undistorted structure (given in parentheses) as follows: $d_{Ru2-Ru2} = 3 \times 2.9284(10)$ Å (2.9766 Å); $d_{Ru2-Sb1} = 2.6194(8)$ Å (2.5778 Å); $d_{Ru2-Sb2} = 3 \times 2.7429(6)$ Å (2.5778 Å); $d_{Ru1-Sb2} = 6 \times 2.6901(8)$ Å (2.9766 Å); $d_{Zn1-Ru2} = 8 \times 2.5361(8)$ Å (2.5778 Å); $d_{Zn2-Ru2} = 4 \times 2.5920(4)$ Å (2.5778 Å); $d_{Zn1-Sb2} = 6 \times 3.263$ Å (2.9766 Å); $d_{Zn2-Sb1} = 2 \times 2.9766(4)$ Å (2.9766 Å); $d_{Zn2-Sb2} = 4 \times 2.9903(4)$ Å (2.9766 Å). These values reveal that the strongest distortion is caused by the displacement of Sb2, which makes six Ru1−Sb2 contacts significantly closer than those in the ideal structure. Associated with the shrinkage is a significant expansion of the corresponding three Ru2−Sb2 (note Ru2 has only four Sb neighbors) and six Zn1−Sb2 contacts. The coordinations of Ru1, Ru2, and Zn2 with Sb2 are indicated in Figure 4 by cyan and olive polyhedra, respectively. Thus, the Ru2−Sb2 and Zn1−Sb2 bonds appear to be weaker than the other Sb−M bonds and are, in the local bonding picture, eventually compensated for by three attractive Ru2−Ru2 and eight Zn1−Ru2 bonds. Remarkably, the distances of the Ru2−Ru2 and Zn1−Ru2 pairs are closer in the distorted real structure than in the ideal one, which is indicative for decisive homo- and heteronuclear intermetallic bonding contributing to the stability of this singular half-Heusler phase.

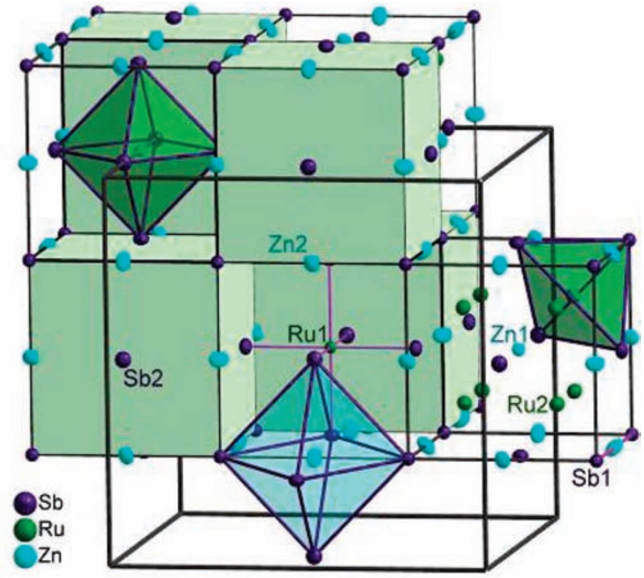

Figure 4. Crystal structure of $Ru_9Zn_7Sb_8$ represented as an alternation of the full-Heusler-type subunit Ru_2ZnSb (solid cubic) and the NaCl-type $RuZn_3Sb_4$ subunit. The coordinations of Ru1, Ru2, and Zn2 with Sb2 are indicated. Thermal ellipsoids are at the 90% probability level.

The ^{121}Sb Mössbauer spectrum confirms the presence of two crystallographic sites of Sb following from the structural analysis (Figure 5). The spectrum was fitted with two different singlets, and the resulting Mössbauer parameters of the two components (A and B) are $\delta_A = -9.068(64)$ mm/s, $A_A = 25.0(1)\%$ and $\delta_B = -7.032(30)$ mm/s, $A_B = 75.0(1)\%$, where δ and A correspond to the isomer shift (relative to $Ca^{121m}SnO_3$ at 4.2 K) and partial intensity, respectively. Taking into account the partial intensities of the subspectra, we attribute sites A and B to the Sb1 (8c) and Sb2 (24e)

---

[18] Slater, J. C. *J. Chem. Phys.* **1964**, *41*, 3199.

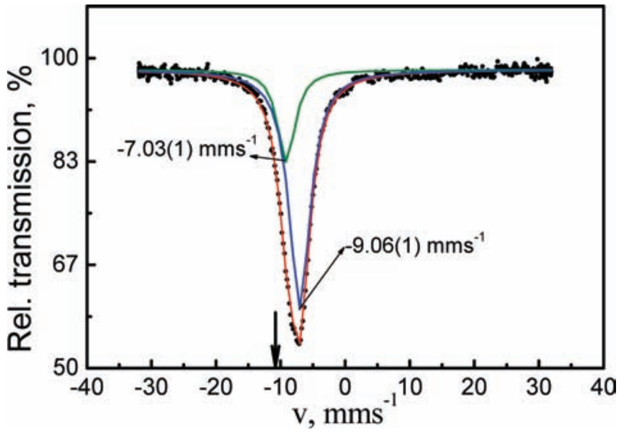

Figure 5. ^{121}Sb Mössbauer spectra of $Ru_9Zn_7Sb_8$ recorded with the source ^{121m}Sn($CaSnO_3$) and absorbers at 4.2 K. The Lorentzian site analysis on the $Ru_9Zn_7Sb_8$ spectrum reveals two Sb sites. As a reference, the line position of Sb metal is indicated by an arrow [δ(Sb) = −10.84 (2) mm/s; T = 4.2 K].

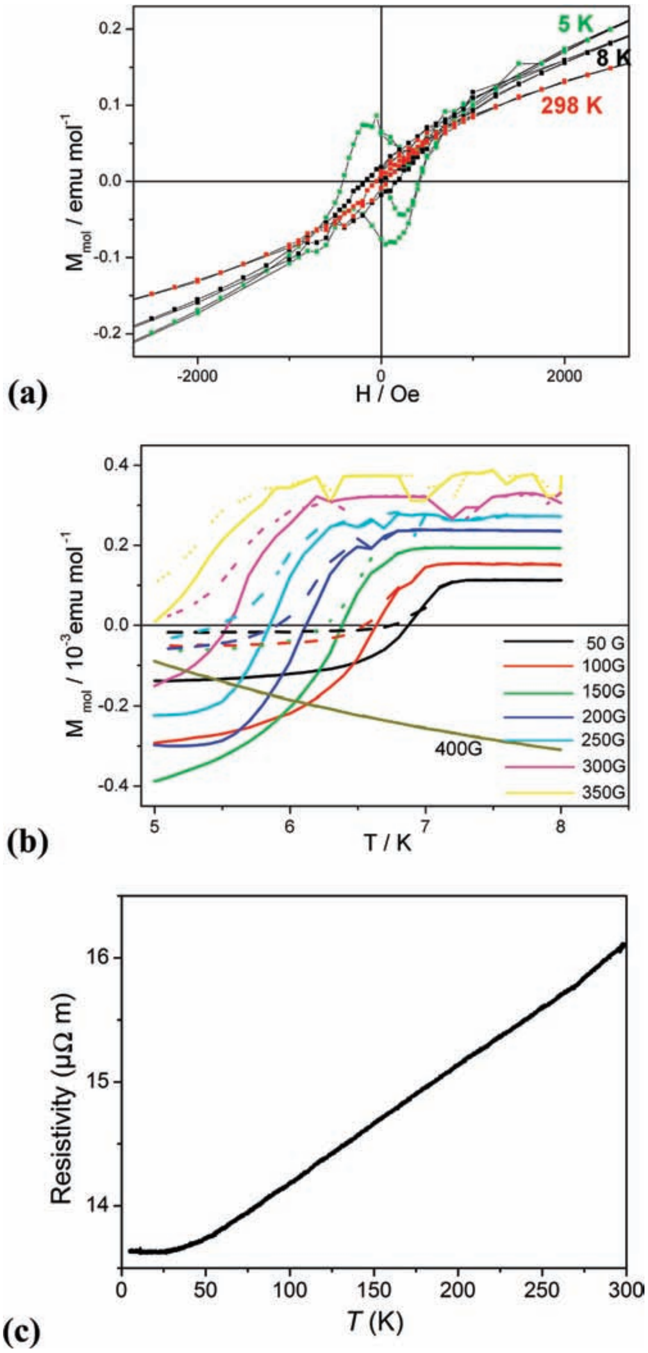

Figure 6. (a) Magnetization M measured at 5, 8, and 298 K as a function of the magnetic field H, indicating a weak ferromagnetism property in $Ru_9Zn_7Sb_8$. (b) Direct-current magnetization, M, measured in zero-field cooling (solid line) and field cooling (dash line) at varied applied field H shown as a function of the temperature, indicating that the Meissner effect is observed at temperatures below 7.2 K in a field of 50 G. Estimating the lower limit of the superconducting volume fraction at 5.0 K from the volume susceptibility, after cooling in an external magnetic field of 50 G, yields about $^1/_{2390}$ of the theoretical value ($-^1/_{4\pi}$). (c) Electrical resistivity in the temperature range down to 2 K.

positions, respectively. Despite displacement of the Sb2 site in $Ru_9Zn_7Sb_8$, there is a zero (or very small) value for the quadrapole splitting, which is different from that of the displaced Sb sites in CoMnSb.[8] The influence from the displacement of Sb2 in $Ru_9Zn_7Sb_8$ is probably weakened by a greater degree of the asymmetric coordination environment than that in CoMnSb and is not sufficient to produce a substantial electric field gradient.

As shown in Figure 6, magnetization measurements on an almost pure specimen (although $RuSb_2$ can be detected by EDS but not in the XRD pattern, as shown in Figure 2) gave hints for the possibility of the coexistence of superconductivity and ferromagnetism in $Ru_9Zn_7Sb_8$, but the electric resistivity measurement (on the other specimen with about 10% impurity, mainly $RuSb_2$) did not show a superconducting transition. These results might give an intuitionistic conclusion that the coexistence comes from impurities. However, magnetic susceptibility measurements on the other three neighboring phases ($Ru_{26}Sb_{24}Zn_{67}$, $Ru_{13}Sb_{12}Zn_{83.4}$, and $Ru_{3.0}Sb_{0.97}Zn_{11.0}$) in the Ru−Zn−Sb system prepared from the same chemical reagents under the same conditions did not indicate superconductivity above 1.8 K,[19] which precludes the possible origin from the starting materials. Meanwhile, the stoichiometric ratio is prone to deviate from $Ru_9Zn_7Sb_8$ and varies at least in the solid solution range $Ru_{9-x}Zn_{7+x}Sb_8$ ($0 \leq x \leq 1$), as indicated by our experiments. Further experiments are necessary to explore the nature of the coexistence and whether the volume fraction of superconductivity can be increased by changing the stoichiometric ratio, as shown in superconductor LiFeAs.[20]

The calculated band structure (Figure 7a) shows that the compound is essentially metallic, and this was confirmed by electrical resistivity and Seebeck coefficient measurement (it is negative, and its absolute value is smaller than 10 μV/K). The bands near the Fermi level (E_F) are mainly composed of d-orbital bands of Ru and p-orbital bands of Sb. The formation of this half-Heusler-type superstructure is controlled by VEC. As shown in Figure 1, no half-Heusler phase with VEC between 8 and 16 was previously reported. The VEC of the nominal composition "RuZnSb" is 15, which is located in the gap in the VEC map. "RuZnSb" has to adjust its VEC to 16 at least in the process of the formation of a half-Heusler-type structure. Because of the similarity in atomic radii (r_{Ru} = 1.325 Å, r_{Zn} = 1.335 Å, and r_{Sb} = 1.45 Å)[18] and the

---

(19) (a) Xiong, D. B.; Habrecht, B. Unpublished results. (b) Xiong, D. B.; Yang, K.; Zhao, Y. F.; Ma, J. *Dalton Trans.* **2010**, *39*, 8331.

(20) Pitcher, M. J.; Lancaster, T.; Wright, J. D.; Franke, I.; Steele, A. J.; Baker, P. J.; Pratt, F. L.; Thomas, W. T.; Parker, D. R.; Blundell, S. J.; Clarke, S. J. *J. Am. Chem. Soc.* **2010**, *132*, 10467.

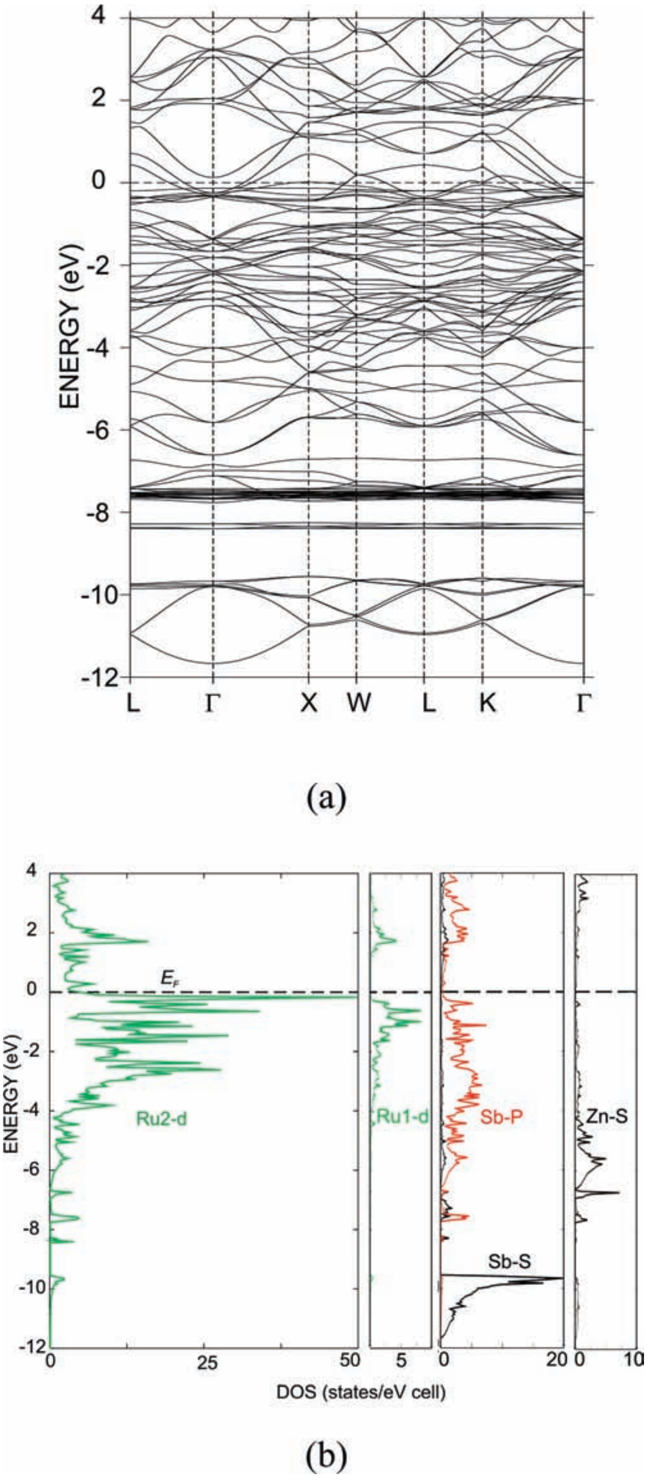

(a)

(b)

Figure 7. Electronic structure of $Ru_9Zn_7Sb_8$: (a) band structure; (b) DOSs.

bigger difference in the number of valence electrons, the adjustment will be realized more easily between Ru and Zn from the viewpoint of energy. To reach the minimum of 16 of VEC, x in $Ru_{1+x}Zn_{1-x}Sb$ should be $^1/_6$ (~0.167), namely, $Ru_{1.167}Zn_{0.833}Sb$, and the ordered $Ru_9Zn_7Sb_8$ ($Ru_{1.125}Zn_{0.875}Sb$) is stabilized by forming the unique superstructure. As we can see from the density of states (DOSs) in Figure 7b, E_F is situated exactly above the large slope contributed by d-orbital bands of Ru2, and 16 is the minimum requirement on VEC for the stability of this superstructure. As was proven in our experiments, the replacement of Ru in $Ru_9Zn_7Sb_8$ by Mn with a poorer electron was not successful, but a Co-containing phase with a richer electron can be prepared, even complete substitution in $Co_9Zn_7Sb_8$. Therefore, $Ru_9Zn_7Sb_8$ is an electronic compound, whose structure is stabilized by maintaining its VEC value.

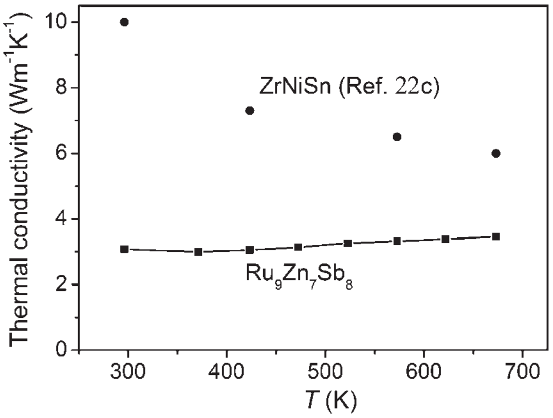

Figure 8. Thermal conductivity of $Ru_9Zn_7Sb_8$ calculated from flash diffusivity measurements. The reported thermal conductivity of ZrNiSn[22c] is given for comparison. The thermal conductivity was calculated by using $\kappa = \rho\alpha C_p$ (W/m·K), where ρ, α, and C_p stand for the mass density, thermal diffusivity, and specific heat, respectively.

Ru2 (32f) occupies the tetrahedral sites of the slightly distorted cubic-closed-packed Sb, and optimized bonds are found in Ru2−Sb1 contacts according to COHP (Figure S2 in the Supporting Information). This local coordination environment resembles that of Fe atoms coordinated tetrahedrally by pnictogens or chalcogens in square-planar sheets in an iron-based superconductor, leading to similarities between their DOSs near E_F.[21] The DOSs near E_F possess a large peak and are dominated by d-orbital bands of transition metals, Ru2 or Fe. The d-orbital band of Ru2 splits into two peaks and is separated by a visible pseudogap, with E_F occurring toward the bottom. However, unlike the direct Fe−Fe interaction in an iron-based superconductor, calculations show the strong antibonding Ru2−Ru2 interaction at E_F because of the corner-sharing $Ru2Sb_4$ tetrahedra like a cuprate superconductor instead of edge sharing in the former.

As indicated by COHP analysis, bondings between Ru1−Sb2 and Zn2−Ru2 are optimized while those between Sb2−Zn1 and Sb2−Zn1 are not, which is in agreement with deduction of the great asymmetric coordination environment around Sb2. The displacement of Sb2 in a distorted real structure was eventually compensated for by these unoptimized contacts to stabilize the structure.

Finally, some brief remarks will be made on the potential of the $Ru_9Zn_7Sb_8$ phases as thermoelectric materials. For most of the normal half-Heusler phases, high thermal conductivity k is one of the shortcomings, decreasing the thermoelectric material performance, such as κ(CoTiSb) > 8 W/m·K,[22a]

---

(21) (a) Lu, D. H.; Yi, M.; Mo, S.-K.; Erickson, A. S.; Analytis, J.; Chu, J.-H.; Singh, D. J.; Hussain, Z.; Geballe, T. H.; Fisher, I. R.; Shen, Z.-X. *Nature* **2008**, *455*, 81. (b) Singh, D. J. *Phys. C* **2009**, *469*, 418.

(22) (a) Barth, J.; Balke, B.; Fecher, G. H.; Stryhanyuk, H.; Gloskovskii, A.; Naghavi, S.; Felser, C. *J. Phys. D: Appl. Phys.* **2009**, *42*, 185401. (b) Kimura, Y.; Zama, A. *Appl. Phys. Lett.* **2006**, *89*, 172110. (c) Muta, H.; Kanemitsu, T.; Kurosaki, K.; Yamanaka, S. *Mater. Trans.* **2006**, *47*, 1453.

κ(HfPtSn) = 14.9 W/m·K,[22b] and κ(ZrNiSn) ≈ 10 W/m·K[22c] at room temperature. Compared with most of the normal half-Heusler phases, the thermal conductivity of $Ru_9Zn_7Sb_8$ is very low (~3 W/m·K) at room temperature (Figure 8), which may be attributed to the structural complexity of this superstructure. Once the lattice thermal conductivity has been lowered, the electronic factors must be addressed. On the basis of the equation[23]

$$S = \frac{\pi^2}{3}\frac{\kappa^2 T}{e}\frac{\mathrm{d}\ln\sigma(E)}{\mathrm{d}E}\bigg|_{E=E_F}$$

the system with rapidly changing DOSs near E_F is expected to have a larger thermoelectric power. As shown in the bottom part in Figure 7, the DOS of $Ru_9Zn_7Sb_8$ varies rapidly near E_F, which is a promising feature for tuning thermoelectrical properties to an optimum, if non-isovalent substitution enables ample values of the Seebeck coefficient and electrical conductivity. This possibility could be expected because of the fact that the composition can vary in a wide range $Ru_{9-x}Zn_{7+x}Sb_8$ ($0 \leq x \leq 1$), indicated by single-crystal XRD and EDS, and analogues $M_{9-x}Zn_7Sb_8$ (M = Fe, Co, Rh) and $Ir_9Zn_7Sn_8$ were also isolated; therefore, its valence electron content can be optimized.

Conclusions

In summary, we have identified the new phase $Ru_9Zn_7Sb_8$ with a unique half-Heusler $2a_{hh} \times 2a_{hh} \times 2a_{hh}$ superstructure, and it is stable up to 1356 K with increasing temperature (Figure S3 in the Supporting Information). The new phase is different from the ordinary half-Heusler phase regarding both stoichiometry and structure, showing abnormal features of atomic coordination against the Pauling rule. Magnetization measurements indicate the coexistence of ferromagnetism and the Meissner effect, but no transition occurs in the electrical resistivity curves, which might be attributed to its very small volume fraction or contributions from impurities. Analogues $M_{9-x}Zn_{7+x}Sb_8$ (M = Fe, Co, Rh) and $Ir_9Zn_7Sn_8$ were also isolated[19a] and are expected to serve as a new structure type for exploring new thermoelectric materials.[2a]

Acknowledgment. D.B.X. thanks the Alexander von Humboldt Foundation (Germany) and Japan Society for the Promotion of Science (JSPS) for fellowships and financial support. Fruitful discussions with Prof. Bernd Harbrecht and his great supports are gratefully acknowledged. We thank Prof. Jürgen Köhler for his help with the electronic structure calculations and Dr. Vadim Ksenofontov for providing the collection and fitting of the Mössbauer spectrum.

Supporting Information Available: Figures S1−S3 (magnetism measurements on different samples, a COHP diagram, and thermal stability), Tables S1−S3 (X-ray crystallographic data), and CIF files. This material is available free of charge via the Internet at http://pubs.acs.org.

---

(23) Mott, N. F.; Jones, H. *The Theory of the Properties of Metals and Alloys*; Dover Publications: New York, 1958.